Substructure heterogeneity during hot deformation of ferritic stainless steels - Experimental characterization and discussion assisted by a mean-field model

Louis Hennocque, Julien Favre, Nicolas Meyer, Thomas Sourisseau, David Piot, Laurence Latu-Romain, Guillaume Kermouche

Substructure heterogeneity during hot deformation of ferritic stainless steels - Experimental characterization and discussion assisted by a mean-field model

Louis Hennocque[1, 2, *1], Julien Favre[2], Nicolas Meyer[1], Thomas Sourisseau[1], David Piot[2], Laurence Latu-Romain[1], Guillaume Kermouche[2]

[1]Centre de Recherches d'UGITECH, Ugine, France

[2]Mines Saint-Etienne, CNRS, UMR5307 LGF, Centre SMS, 42023 Saint Etienne, France

Abstract

The microstructure evolution of ferritic stainless steels during hot deformation is complex and needs to be finely described. Quantifying the evolution of the misorientation of low-angle boundaries depending on the thermomechanical path is a key point in controlling the recrystallization of such steels. This paper proposes an experimental methodology based on large-scale electron back-scattered diffraction (EBSD) mapping characterization using a Symmetry 2 camera to track the low-angle boundary evolution. Different thermomechanical paths, from 900 to 1100 °C with strain from 0.3 to 0.9, were studied using uniaxial compression tests. Flow stress follows a usual hardening stage, followed by a slight softening regime, mostly attributed to continuous dynamic recrystallization. Distributions of low-angle boundary populations (density vs sub-grain size) are quantified by two populations either near grain boundaries or inside grain bulk; the proportion of sub-grains at grain boundaries increases with strain. These results are discussed using the mean-field model of Gourdet-Montheillet. This model is insufficient to capture the transient stage of continuous dynamic recrystallization unless its set of parameters is adjusted to accommodate the saturation of the density of low-angle boundaries near grain boundaries. This saturation is a result of the low-angle boundary density gradients in the grains.

Keywords: characterization, modelling/simulations, iron alloys, electron microscopy, grains, and interfaces

I. Introduction

Hot deformation of ferritic steels implies a significant change in microstructure, driven by the combined effects of recovery and recrystallization. Effective prediction of these phenomena through models can enable substantial control over the microstructure. A precise description of these processes requires an accurate understanding of the subgrain structure involved. The density of Low Angle Boundaries (LAB) created during deformation, with recovery and Continuous Dynamic Recrystallization (CDRX) mechanisms, is specific to materials with high stacking fault energy (SFE) [1], [2], [3]. For these materials, dynamic recrystallization does not result in the nucleation phenomena that can be observed for low SFE materials such as copper or austenitic grades. Instead, a progressive increase in LAB misorientation can lead to High Angle boundaries (HAB) [2]. To describe the microstructure changes during hot deformation,

[1]Corresponding author.
E-mail address : (L. Hennocque)

it is necessary to quantify the LAB density - i.e. the total length of LAB per unit area - and track the evolution of its misorientation as a function of temperature, strain rate, and deformation. These two properties can be identified with appropriate characterization and are widely referenced in the literature to identify key parameters linked to CDRX phenomena [1], [3], [4], [5]. LAB density provides an estimation of subgrain size while monitoring its misorientation allows the quantification of surface energy. Surface energy and subgrain size are two parameters that need to be known for the prediction of potential nucleation events [6], [7], [8].

The quantification of LAB density and the misorientation distribution are usually investigated at the global scale of the polycrystal, assuming homogeneous average values [1], [5], [9]. However, plastic deformation starts at the grain boundary, resulting in strain gradients in the grains [3], [10]. These gradients induce a heterogeneous LAB distribution, with a higher density near grain boundaries [10]. Previous works [11], [12] have discussed about this local texture and highlighted the disparities that can exist at the grain scale. However, few quantifications of misorientation distributions and LAB densities have been done at the grain scale with a consideration of gradients.

For more than twenty years, CDRX model [1], [4], [13], [14], [15] has been successfully used to predict microstructure evolution in the steady state regime on various materials with high SFE. This model was improved by considering alternative approaches; some authors have distinguished different contributions of dislocation densities [5], [9], [15], [16], [17]. These models provide a better prediction in the transient stage, however at the expense of a large number of parameters to be identified. Therefore, a simpler approach still missing for an accurate description of the microstructure change during the transient stage, with a proper consideration of LAB density gradients.

The goal of this paper is twofold. First, it attempts to capture the evolution of LAB heterogeneity through an extensive experimental series of hot-compression tests. Then, the original CDRX model was revised and parameters were redefined to accurately describe the LAB population at different scales. This work yields an accurate description of both LAB density and misorientation distribution while preserving a low number of parameters to identify.

II. Materials and methods

Material

The material, whose composition is detailed in Table 1, was a Niobium-free ferritic stainless steel. It is close to classical AISI 430, but with a higher Cr amount, slightly above 18 wt%, and low C, N contents intended to have a fully ferritic structure across the hot working temperature range.

Table 1: Composition of studied ferritic stainless steel:

Type	C	Si	Mn	Ni	Cr	Mo	V	Cu	S	P	N	Nb	O (ppm)
Wt (%)	0.006	0.375	0.334	0.127	18.25	0.02	0.053	0.021	0.003	0.021	0.014	0.008	40

The grade was developed from elemental metals by Ugitech. The as-received material was smelted in a Vacuum Induction Melting (VIM) furnace and then cast into a 25 kg ingot. The latter was forged into bars of section 18 mm x 38 mm. Finally, heat treatment of 40 minutes at 900 °C interrupted by water quenching was carried out on the bars to ensure a fully recrystallized state. The final microstructure presents an initial grain size of 80 µm. Cylindrical samples, measuring 19.5 mm in height and 13 mm in diameter, were machined from the forged bar. The long axis of the specimen was oriented parallel to the rolling direction.

Hot deformation

Uni-axial compression of these samples was carried out using a computer-controlled Schenck servo-hydraulic machine. To maintain a constant temperature in the test piece without any thermal gradients, an infrared radiation furnace was employed. Two thermocouples, inserted in both compression anvils, were used to control the sample's temperature. Additionally, the system features a mechanical quenching system for rapid ejection and cold water quenching after deformation. To reduce friction during deformation, a graphite-based lubricant was used. A holding time of 10 minutes was applied before deformation to ensure a homogeneous temperature. Compression tests were carried out at temperatures of 900 °C, 1000 °C, and 1100 °C with a true strain of 0.3 up to 0.9, and a strain rate of 1 /s. Also, a compression test was conducted at 1000 °C, with a strain of 0.6, at 0.01 /s. The flow stress values were corrected to consider the effect of friction with the anvils. The correction was applied using a Tresca friction coefficient $\bar{m} = 0.05$ [4], [18]. Adiabatic self-heating was estimated and taken into account for the different stress-strain curves considering that 90 % of mechanical energy is retained in the compression specimen and contributes to the temperature increase [19].

Microstructure characterization

Cross-sections through the center of the compressed samples were prepared for characterization by EBSD. The samples were cut by Electrical Discharge Machining (EDM). A standard metallographic preparation was done by mechanical polishing to a final grade of P4000 (5 µm SiC granulometry) followed by electropolishing with 10% $HClO_4$ and 90% ethanol solution for 30 seconds at 32 V at ambient temperature.

The microstructure observations were carried out on a Zeiss scanning probe microscope (SEM) equipped with a FEG (Field Emission Gun) tip, model Supra 55 VP. EBSD analysis was conducted with a Symmetry 2 camera with a CMOS (Complementary metal-oxide-semiconductor) detector from Oxford Instruments NanoAnalysis. EBSD data was collected using AztecHKL software. To reconcile sufficiently large statistics with the fine characterization of substructure evolution, a trade-off was done with a sufficiently small step size of 1 µm, and an analysis over a large area of 2.5 mm^2. Various possible camera modes allow for selecting the image size. For the presented characterizations, the second mode is used, which corresponds to an image size of 156×128 pixels.

EBSD data were post-processed using MTEX, a free Matlab toolbox for analyzing and modeling crystallographic textures using EBSD data.

Minimum misorientation was taken at 1°, and lower values were disregarded. Below this threshold, the measurement is affected by the measurement noise.

A grain is defined as any closed contour of boundaries whose misorientation is greater than 15°. On the other hand, a subgrain is defined by boundaries with misorientation ranging from 1 to 15°, inclusive.

The lowest size limit for detecting and taking into account subgrains is set at 10 pixels.

The subgrain population is extracted from EBSD data using the calcGrains function of the MTEX toolbox. The dataset is post-processed using Python Scikit libraries . The subgrain population is analyzed using the Gaussian Mixture Model function of Scikit [19].

Numerical approach

The CDRX model is set based on the works of Gourdet and Montheillet [1]. It relies on the computing of the subgrain size, misorientation distributions, and dislocation density. The main model inputs are the deformation conditions (temperature, deformation, deformation rate). The input also includes the intrinsic material properties, such as hardening and dynamic recovery parameters, migration rate, and the initial grain size.

The following variables are used to track the microstructure evolution:

- The density of dislocations within the i-th subgrain, denoted as ρ_i,
- The surface area of boundaries (grain and subgrain boundaries) per unit volume, denoted as S_v. It is linked to the average size of crystallites, D, through the stereological relationship D=2/ S_v [20]
- The misorientation of subgrains is defined by the misorientation function $\varphi(\theta)$.
- $\varphi(\theta)d\theta$ represents the surface fraction of subgrains with misorientation ranging between θ and $\theta+d\theta$.

The surface fraction of subgrains f_{LAB} is given by:

$$f_{LAB} = \int_{\theta_0}^{\theta_c} \varphi(\theta)\, d\theta \tag{1}$$

where θ_0 and θ_c represent, respectively, the minimum disorientation angle of the subgrain and the critical disorientation angle beyond which the boundary is regarded as a grain boundary. θ_0 and θ_c are considered as 1° and 15°, respectively.

The evolution of dislocation density within the subgrains is influenced by hardening, dynamic recovery, and the migration of grain boundaries. The dislocation density is governed by the Laasraoui-Jonas relation [21], modified to account for boundary migration:

$$d\rho_i = (h - r\rho_i)d\varepsilon - \rho_i dV \tag{2}$$

where h (m^{-2}) and r (dimensionless) are respectively the hardening and dynamic recovery parameters, dV being the volume) swept by grain boundaries (written as the product of HAB area per unit volume and the distance for a time increment). One hypothesis of the model is that LAB mobility is negligible, and only HAB migration is considered through the term dV. The

parameters *h* and *r* are determined using a numerical method presented in previous works [22]. The variations of h and r can be expressed with the strain rate and temperature according to the empirical relationships [4], [23]:

$$r = r_0 \dot{\varepsilon}^{-m_r} e^{-\left(\frac{m_r Q_r}{RT}\right)} \tag{3}$$

$$h = h_0 \dot{\varepsilon}^{m_h} e^{\left(\frac{m_h Q_h}{RT}\right)} \tag{4}$$

Where h_0 (m^{-2}) and r_0 are pre-exponential constants, m_h and m_r are strain rate sensitivity parameters, and Q_h(kJ.mol^{-1}) and Q_r(kJ.mol^{-1}) are activation energy factors for *h* and *r*. The values are presented in the Table 2, and determined from previous work [22]:

Table 2: Parameters for the determination of h and r

Rheological parameters	h_0 (m^{-2})	r_0	m_h	m_r	Q_h(kJ.mol^{-1})	Q_r(kJ.mol^{-1})
	3 x 10^{12}	362	0.49	0.02	103	1963

The negative contribution of boundaries migration *dV* is written as:

$$dV = \frac{2 f_{HAB} c_2 v_{HAB}}{D \dot{\varepsilon}} d\varepsilon \tag{5}$$

Where v_{HAB} represents the migration velocity of mobile grain boundaries depending on experimental conditions, c_2 is an adjustment parameter (dimensionless), f_{HAB} the fraction of grain boundaries in the system, equivalent to (1-f_{LAB}), and *D* is the subgrain size.

The model assumes that dislocations are eliminated through dynamic recovery $r\rho_i d\varepsilon$ following two ways. First, a fraction α creates a new LAB with minimal misorientation θ_0. Secondly, the remaining fraction $(1 - \alpha)$ is lost into existing boundaries, contributing to the increase of their misorientation and the transformation of subgrains into grain boundaries.

Additionally, the misorientation increase $d\theta$ is calculated by:

$$d\theta = \frac{1}{c_1}\frac{b}{2n}.(1-\alpha)\ r\ \rho_i D \mathrm{d}\varepsilon \tag{6}$$

c_1 is an adjustment parameter (dimensionless). An increase in LAB surface area dS^+ is created with a misorientation θ_0 during the deformation increment dε:

$$dS^+ = \frac{1}{c_1}\frac{b}{n\theta_0}\alpha r \rho_i d\varepsilon \tag{7}$$

where *b* is the Burger vector (m), and *n* is the number of dislocation families per sliding plane. *r* is the dynamic recovery parameter of Equation (5), ρ_i the dislocation density (m^{-2}). On the

other hand, the movement of mobile grain boundaries causes a decrease $dS^- = SdV$ in LAB surface area:

$$dS^- = f_{HAB} S^2 \, v_{HAB} c_2 \frac{d\varepsilon}{\dot{\varepsilon}} \quad (8)$$

where S is the variation in LAB density (m/m^2), v_{HAB} is the migration velocity of grain boundaries (m.s^{-1}), and $\dot{\boldsymbol{\varepsilon}}$ the strain rate (s^{-1}). c_1 and c_2 are parameters that are not taken into account in the original model of Gourdet-Montheillet. These additional parameters allow us to modulate the amplitude of each equation, and their determination will help to understand the effective contribution of each mechanism. The parameter values and their consequence on the physical understanding of CDRX are discussed in the next section.

III. Results

Microstructure characterization after hot testing

Figure 1 shows the compression curves for T=900, 1000, and 1100 °C and ε= {0.3, 0.6, and 0.9} at 1 s^{-1}, and a compression curve at 1000 °C for a strain of 0.6 at 0.01 s^{-1}. Stress obtained for the different strains is presented in Tableau 3. The uncertainties are calculated directly from the standard deviations (measured for the same-targeted conditions).

Tableau 3: Stress values at different strains and different temperatures

	900 °C	**1000 °C**	**1100 °C**
ε=0.3 (± 0.02)	94 ± 1 MPa	56 ± 1 MPa	36 ± 1 MPa
ε=0.6 (± 0.01)	95 ± 2 MPa	58 ± 0.3 MPa	36 ± 1 MPa
ε=0.9 (± 0.06)	87 MPa	53 MPa	34 MPa

The end of the elastic range is characterized by σ_0. The hardening range of the stress-strain curve starts at the end of this elastic range and ends at the maximum stress $\sigma_{max.}$ Both σ_0 and σ_{max} values are presented in Tableau 4.

Tableau 4 : σ_0 and σ_{max} for 900, 1000 and 1100 °C

	900 °C	**1000 °C**	**1100 °C**
σ_0 (MPa)	72 ± 1	41 ± 1	24 ± 1
$\sigma_{max.}$ (MPa)	92 ± 2	57 ± 0.3	35 ± 1

Beyond σ_{max}, the beginning of a softening range is observed, as the stress decreases.

For the compression test at 0.01 s^{-1}, a maximum of 19 MPa is quantified and displays a stress shift of 38 MPa compared to the test at 1 s^{-1}, eps = 0.6, and 1000 °C.

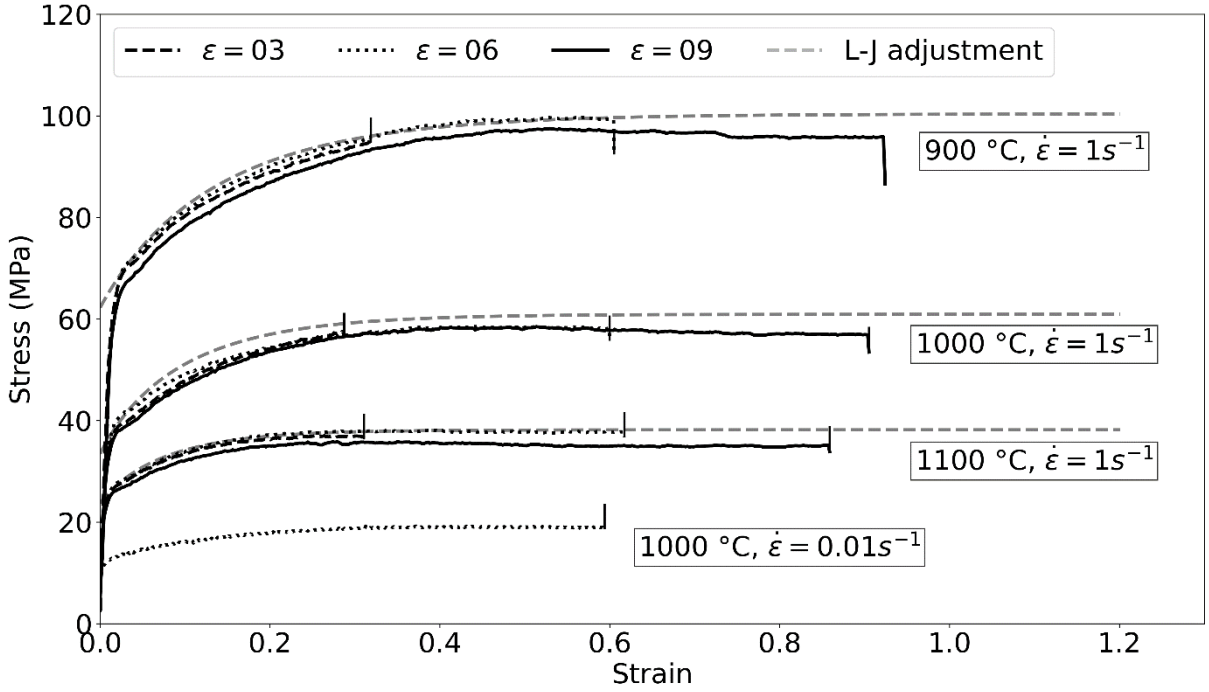

Figure 1: Evolution of stress (σ) as a function of strain (ε). For three levels of deformation at 900, 1000, and 1100 °C for $\dot{\varepsilon}$ = 1 s^{-1}, as well as the curve at 1000 °C at ε = 0.01 s^{-1}, ε = 0.6. The vertical lines act as indicators marking the end of the deformation. Numerical adjustments obtained with Laasraoui-Jonas (L-J) are plotted for 900, 1000, and 1100 °C.

Determining h and r (equations (3) and (4)) in Table 2 allows the corresponding numerical adjustments for 900, 1000 and 1100 °C to be plotted.

Figure 2 shows the microstructural evolution depending on strain, at 900 °C and 1 s^{-1} after hot compression tests. Grains boundaries (GB) are shown in black, and low-angle boundaries (LAB) are highlighted in red for misorientations from 1 to 15 degrees excluded. Figure 2. a-c) represents only the grain boundaries and band contrast (BC), while Figure 2. d-f) also shows the superposition with the LAB (red lines). As the deformation increases, grains elongate perpendicular to the compression axis, leading to an increased aspect ratio and a higher density of grain boundaries observed on the map. As deformation increases from 0.3 to 0.9, so does the LAB density.

Moreover, LABs are preferentially located in the vicinity of the grain boundaries. At low deformations (ε=0.3, Figure 2.d), heterogeneity is the most pronounced, and decreases with the deformation, until it is barely visible at the maximum characterized deformation (ε=0.9, Figure 2. f).

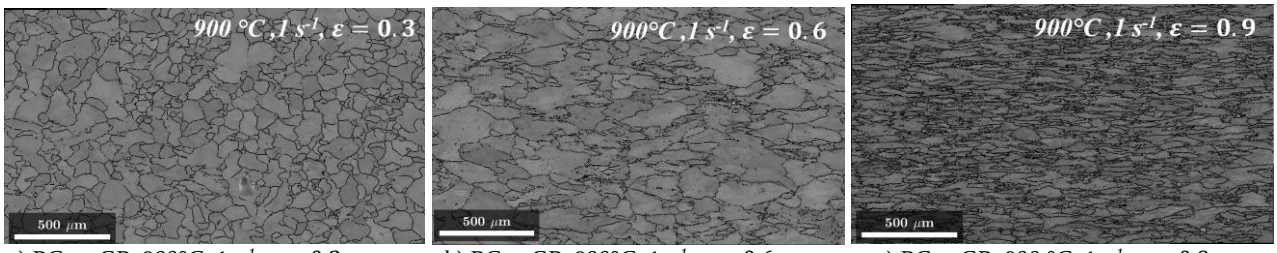

a) BC + GB, 900°C ,1 s^{-1}, ε = 0.3 *b) BC + GB, 900°C ,1 s^{-1}, ε = 0.6* *c) BC + GB, 900 °C ,1 s^{-1}, ε = 0.9*

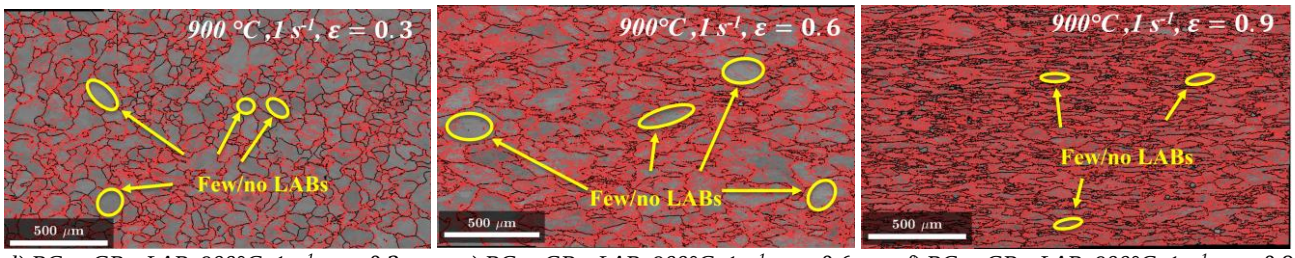

d) BC + GB +LAB, 900°C ,1 s^{-1}, ε = 0.3 *e) BC + GB +LAB, 900°C ,1 s^{-1}, ε = 0.6* *f) BC + GB +LAB, 900°C ,1 s^{-1}, ε = 0.9*

Figure 2: EBSD band contrast maps combined with HAB (with misorientation superior or equal to 15°, black lines) –top- with LAB (with misorientation from 1 to 14°, red lines) –bottom- for hot deformation at 900 °C with deformation of 0.3; 0.6; 0.9 with 1 s^{-1} strain rate.

The LAB distribution in the microstructure was also characterized for different temperatures (900, 1000, and 1100 °C). Figure 3 shows the microstructure evolution for temperatures varying from 900 to 1100 °C with a fixed strain at 0.6 (Figure 3a-b) and two strain rates (either 0.01 or 1 s^{-1}, Figure 3c-d). As the temperature increases, so does grain size. LAB density decreases as the temperature increases, as shown in Figure 3c-d. These two trends are associated with a joint effect of recovery, recrystallization, and boundary migration, resulting in larger grains with a

lower LAB density. The microstructure at 1100 °C shows static recrystallization, with equiaxed large grains free of any LAB on the EBSD map (white arrows in Figure 3).

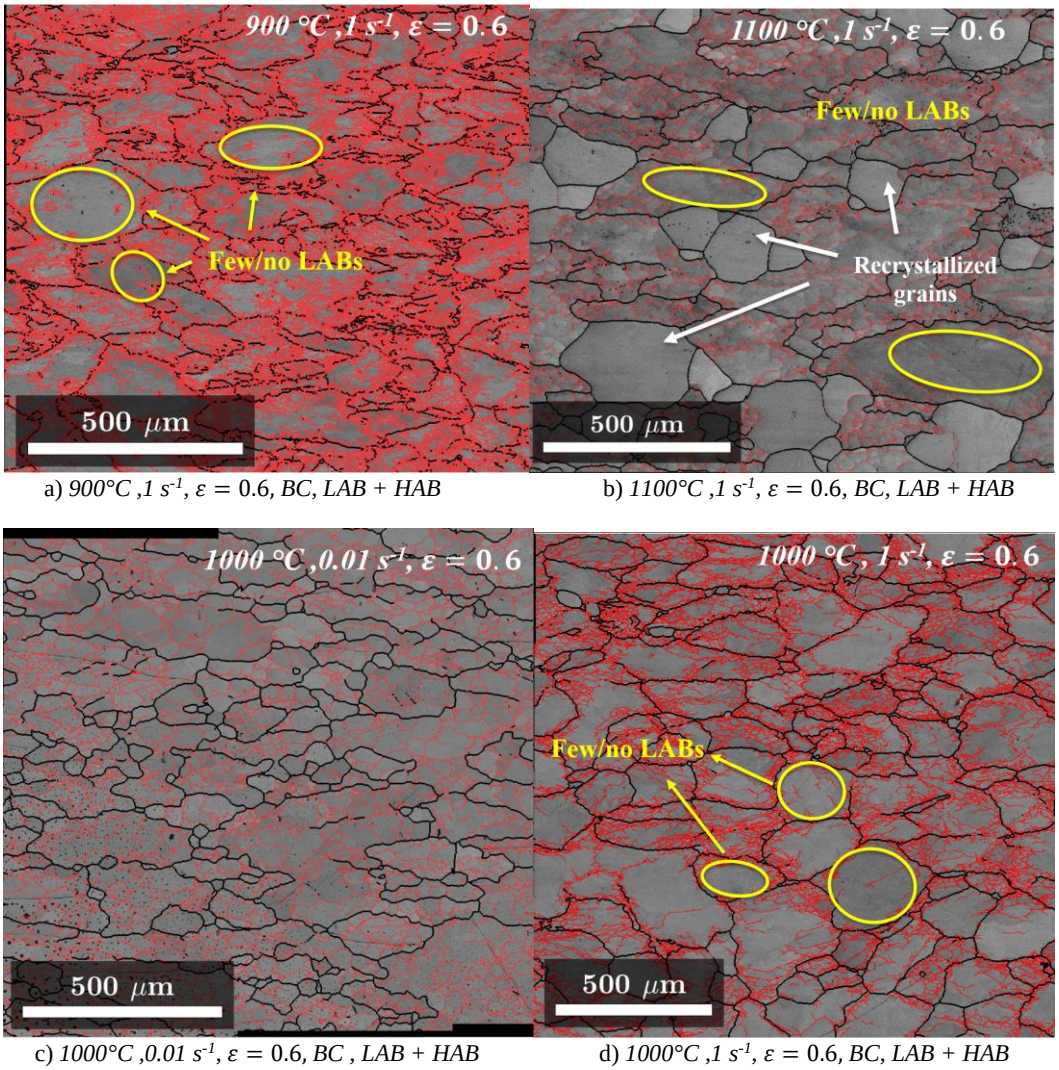

a) *900°C ,1 s^{-1}, ε = 0.6, BC, LAB + HAB* b) *1100°C ,1 s^{-1}, ε = 0.6, BC, LAB + HAB*

c) *1000°C ,0.01 s^{-1}, ε = 0.6, BC , LAB + HAB* d) *1000°C ,1 s^{-1}, ε = 0.6, BC, LAB + HAB*

Figure 3: EBSD band contrast maps combined with HAB (with misorientation superior or equal to 15°, black lines) and LAB (with misorientation from 1 to 14°, red lines) for 900 °C a) and 1100 °C b), for 0.01s^{-1} c) and 1s^{-1} d) for hot deformation of ε=0.6

The presence of recrystallized grains can be associated with the quenching process after deformation, lasting a few tenths of a second. The analysis of LAB will be restricted to deformed grains solely, by considering a partition of the EBSD maps. This analysis aims to capture the effect of dynamic recovery on the genesis of the LAB network. The subsequent recrystallization occurring during the quenching step will be investigated separately in future works.

Regardless of the temperature, at a strain rate of 1 s^{-1} (Figure 1 and Figure 3. a-b-d), the LABs are less present in grain volume than at grain boundaries (different grains and circles are shown to illustrate it, with yellow arrows and circles). However, at a lower strain rate of 0.01 s^{-1}, for 1000 °C, heterogeneity is less noticeable, and LAB spread more homogeneously over all the volume of grains.

Study of microstructure: global quantified analysis over the polycrystal

The LAB densities are measured by dividing the total length of low-angle boundaries by the total area of deformed grains shown on the EBSD map. The graph in Figure 4.a shows the evolution of the overall LAB density for different temperatures, depending on deformation. With increased deformation, the density tends to level off, for $\varepsilon > 0.6$ (Figure 4. a). This observation is consistent with the transition between hardening and softening quantified on different experimental stress-strains curves (Figure 1). At low strain levels, the hardening is predominant, resulting in a joint increase of flow stress and LAB density. For $\varepsilon>0.6$, a balance between hardening and dynamic recovery is met, resulting in a stabilization of both flow stress and LAB density. As temperature increases, the increase of LAB density with strain is lower. This can be attributed to the lower dislocation density level contributing to a lesser extent to the creation of LAB by dS^+ in equation (7).

Misorientations distributions (φ) of the different characterizations are shown in Figure 4 (from b. to d). These distributions are plotted by calculating misorientation on a pixel-by-pixel basis. The distributions φ decrease with misorientation, from 1 to 14 °. There is little change in misorientation distributions depending on temperature (Figure 4 from b. to d). The majority of the LABs are composed of low misorientations (i.e. in Figure 4. b, there is almost 60% of the LABs disoriented between 1 and 2 degrees).

As deformation increases, φ tends to increase its average misorientation, with a shift of the distribution to higher values. In Figure 4, from b. to d., i.e. for 900 °C the mean misorientation is 1.8 °, 2.3 ° and 3 ° for deformation of 0.3, 0.6, and 0.9 respectively.

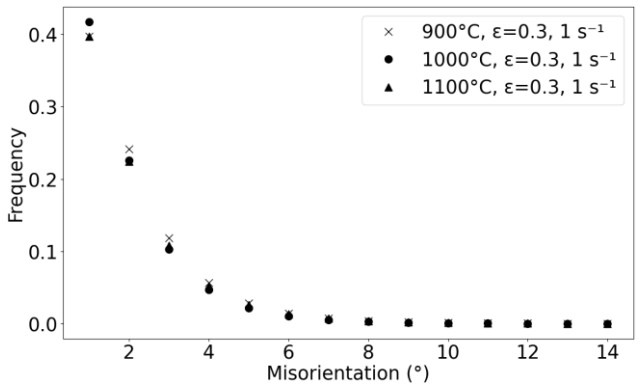

b) Misorientation distribution at $\varepsilon = 0.3$

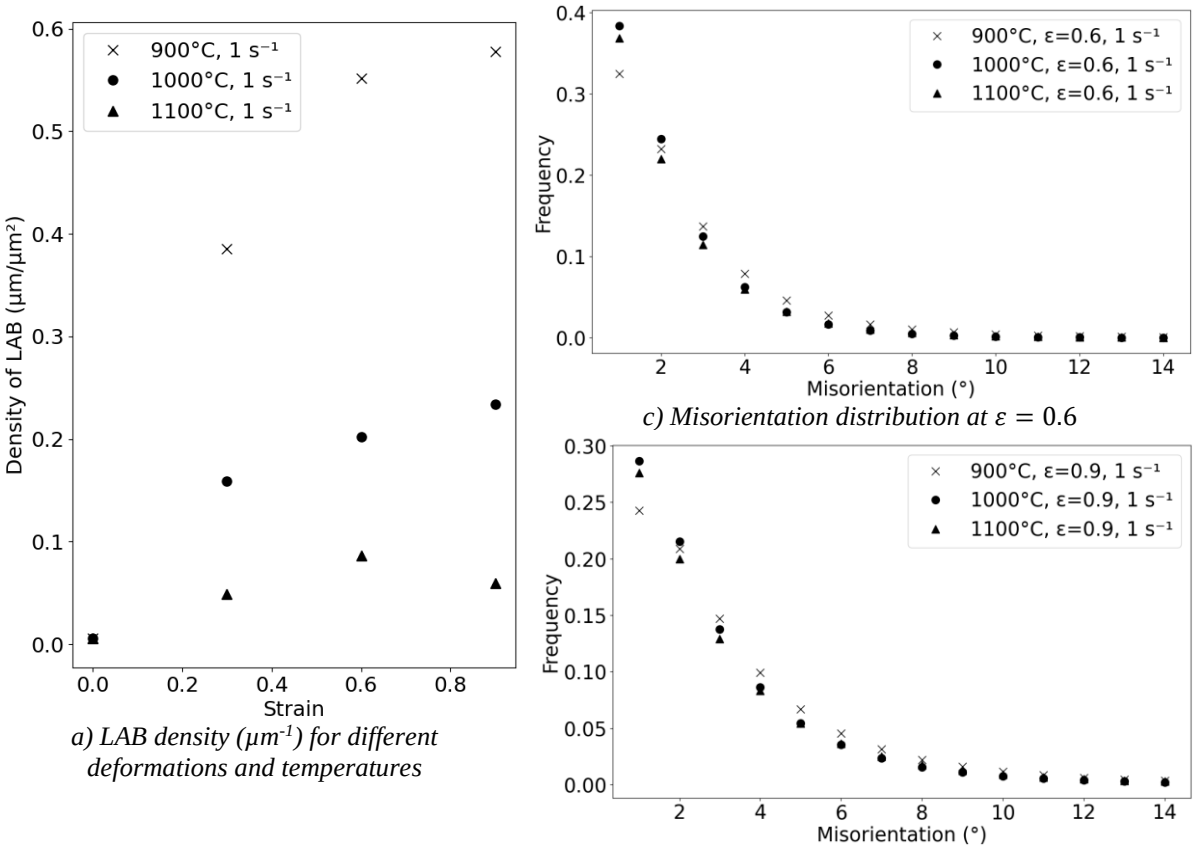

a) LAB density (μm^{-1}) for different deformations and temperatures

c) Misorientation distribution at $\varepsilon = 0.6$

d) Misorientation distribution at $\varepsilon = 0.9$

Figure 4: a) Evolution of LAB density and b-d)- Evolution of misorientation distribution for 900,1000 and 1100 °C and $\varepsilon = \{0.3, 0.6, 0.9\}$

Study of closed contours: subgrains analysis

To characterize the heterogeneity shown in Figure 2 and Figure 3. a-b-d, focus is made only on the subgrains. Subgrains are defined thereafter as crystalline entities delimited by a close contour in the LAB network. These subgrains are of specific interest: due to their closed morphology, they may constitute independent crystalline entities that may evolve later in the deformation process, either by boundary migration due to capillary forces, or even by nucleation of new grains during recrystallization. Such phenomena are less likely for other LABs due to a lower boundary curvature and fewer connections to the LAB network, resulting in lower expectations for subsequent evolutions. This section will focus on the specific evolution of these subgrains.

Figure 5 shows an example of a post-processing that compares a microstructure with all LAB present in the microstructure (red lines in Figure 5a) compared to those forming subgrains (red lines in Figure 5b). Of course, the amount of LAB highlighted in Figure 5b is lower, as not all the LAB are contributing to the delimitation of closed subgrains.

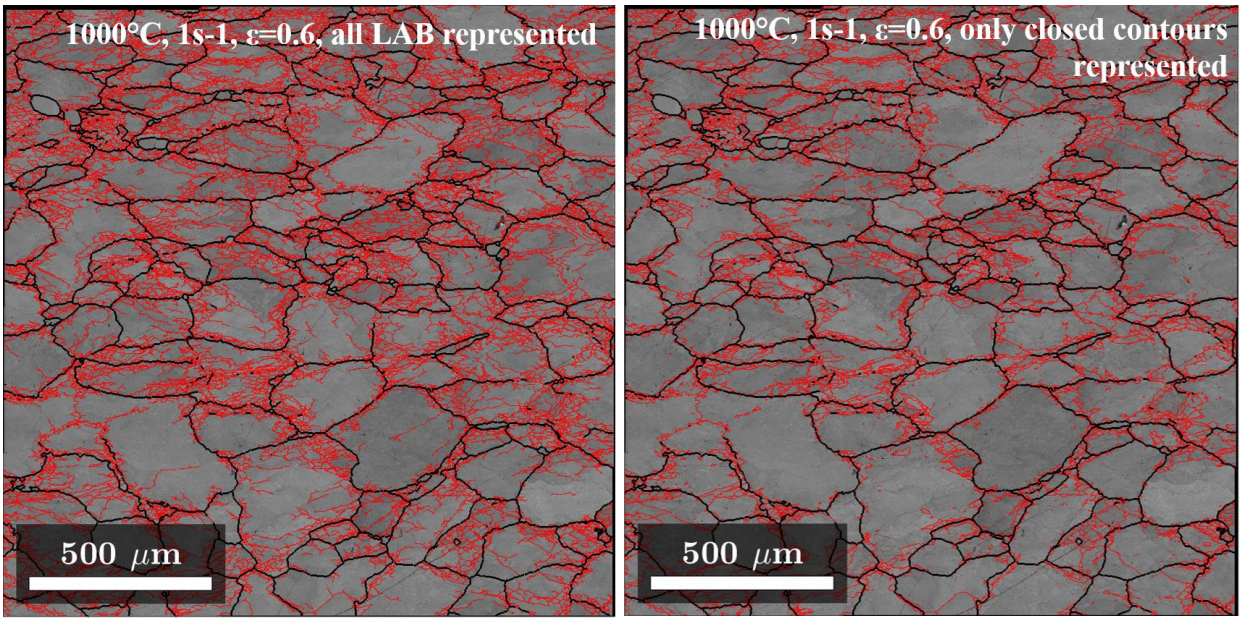

a) Representation of all the LAB present *b) Representation of the closed contours*

Figure 5: EBSD band contrast maps with grains boundaries (with misorientation superior or equal to 15°, black lines) and LAB (with misorientation from 1 to 14°, red lines) a) Representation of all the LAB on the map and only the closed contours b) for 1000 °C, with a strain rate of $1s^{-1}$, at ε=0.6

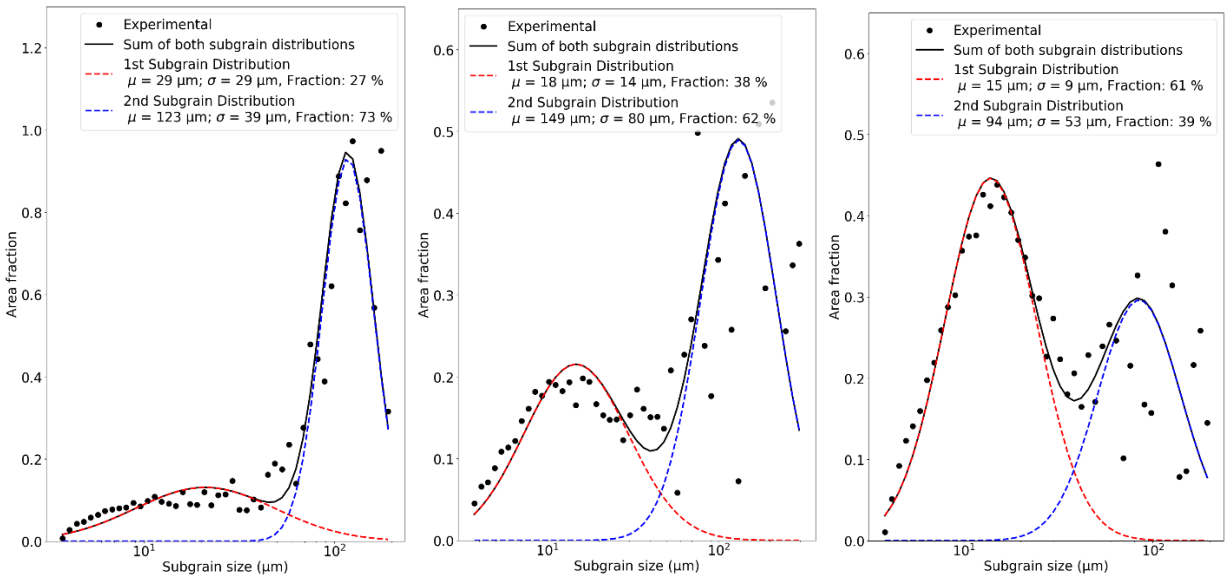

a) 1000°C ,1 s^{-1}, ε = 0.3, GMM subgrain distribution

b) 1000°C ,1 s^{-1}, ε = 0.6, GMM subgrain distribution

c) 1000°C ,1 s^{-1}, ε = 0.9 GMM subgrain distribution

Figure 6: Bimodal distribution of the subgrain population representing area fraction as a function of subgrain size with the mean (μ) and standard deviation (σ) associated with the two distributions detected shows the subgrains distributions at 1000 °C with strain from ε=0.3 to ε=0.9.

The subgrain size follows log-normal distributions, as can be seen by the Gaussian shape in Figure 6 with a size axis following a log scale. However, these distributions are composed of the superposition of two log-normal distributions, constituting two distinct modes in the population of subgrains. It is proposed to quantify these two distribution modes using a Gaussian Mixture Model (GMM). GMM is a probabilistic algorithm used to model dataset distributions by a linear combination of normal distributions. Here the same method is applied, with log-normal distributions. The resulting deconvolution of the two modes is illustrated in Figure 6 by the red and blue log-normal distributions.

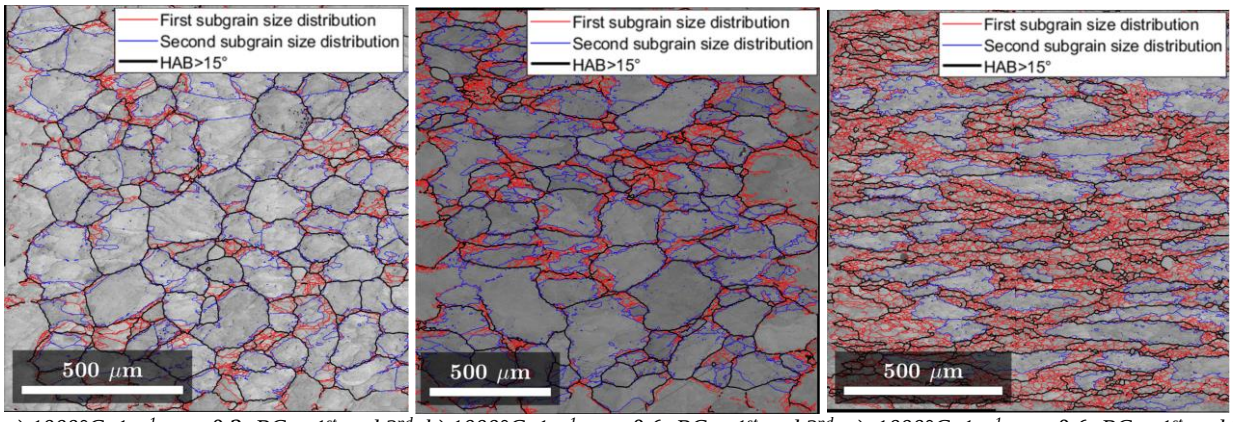

a) 1000°C ,1 s^{-1}, $\varepsilon = 0.3$, BC + 1st and 2nd subgrain distributions (red and blue lines) *b) 1000°C ,1 s^{-1}, $\varepsilon = 0.6$, BC + 1st and 2nd subgrain distributions (red and blue lines)* *c) 1000°C ,1 s^{-1}, $\varepsilon = 0.6$, BC + 1st and 2nd subgrain distributions (red and blue lines)*

Figure 7: Corresponding representations of the two subgrain modes determined at 1000 °C

The subgrain mode illustrated in red has the lowest mean size value, typically in the range of 15 – 30 µm depending on conditions. It corresponds mostly to subgrains lying on grain boundaries, as illustrated by red lines in Figure 7a-c. The second distribution mode illustrated in blue in Figure 7a-c corresponds to LAB marked in blue on the EBSD map. For this second mode, the larger subgrains are located in the undeformed part of the grains.

Figure 8. a shows the mean size and the amplitude of the first mode as a function of temperature for strain levels from 0.3 to 0.9. As temperature increases, subgrains of the first mode tend to increase their size. For example, subgrain size increases from 12 microns at 900 °C to 79 microns at 1100 °C for $\varepsilon = 0.3$. This size increase can be attributed to two factors. First, the increase in temperature results generally in lower LAB densities, and this remains true for this smaller mode as well, resulting in larger subgrain sizes. Moreover, some possible subgrain migration and coalescence cannot be excluded, and such phenomena may contribute to the increase in the subgrain size at higher temperatures.

As deformation increases from 0.3 to 0.6, subgrains tend to decrease in size, with a stabilization beyond a deformation of 0.9. This confirms the primary role of strain on the reduction of subgrain size, well reported in the literature [24], due to the increase of LAB density with deformation.

In Figure 8. b, the relative amplitude of the two subgrain modes is presented. For a constant temperature of 900 °C, the relative fraction of the first mode is 0.34, 0.59, and 0.7 for deformations of 0.3, 0.6, and 0.9, respectively. For a constant deformation (e.g., ε = 0.9), the fraction is observed as 0.7, 0.61, and 0.48 at temperatures of 900, 1000, and 1100 °C, respectively. These trends confirm that the first mode of subgrains tends to increase significantly at higher strain and lower temperature, in processing conditions where strain

hardening is especially high and results in larger LAB density values. Therefore it confirms that the first size mode is well associated with the subgrains formed during plastic deformation of grains.

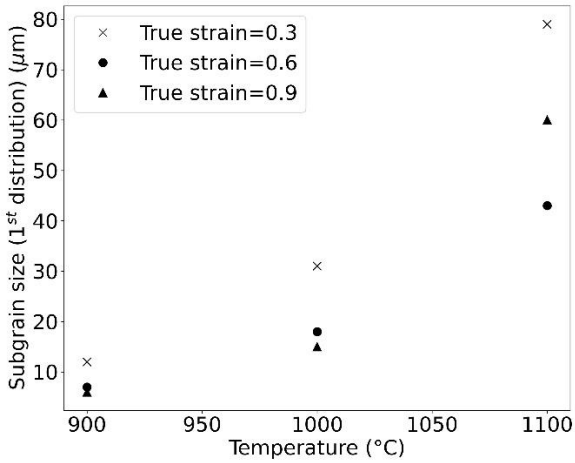

a) *Evolution of subgrain size of the first subgrain mode depending on the temperature for different strains*

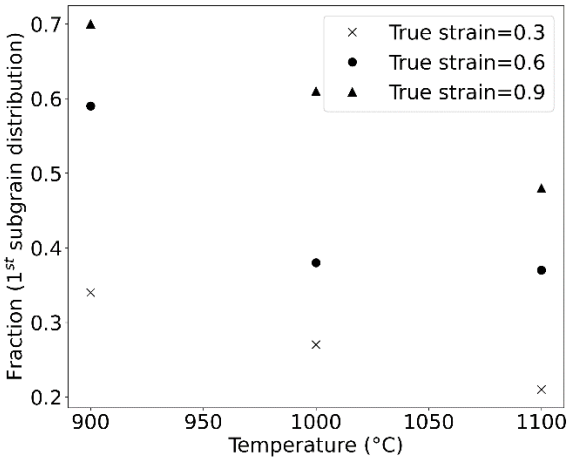

b) *Evolution of the relative fraction of the first subgrain mode as a function of temperature*

Figure 8: (a) Size and (b) fractions of subgrain population (1st mode) for $\varepsilon = \{0.3; 0.6; 0.9\}$ *at T = {900, 1000, 1100} °C*

The same analysis as the one presented in Figure 4a-d is applied to the LAB population restricted to the first mode of subgrains only (red lines of Figure 7d-f). To represent the LAB density associated with these subgrains, denoted S_{Local}, a correlation between subgrain size and LAB density was utilized, written as $S_{Local} = 2/d_{first\ mode}$

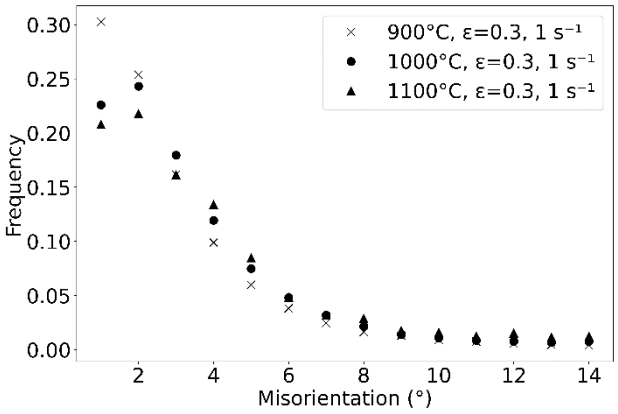

b) Misorientation distribution at $\varepsilon = 0.3$

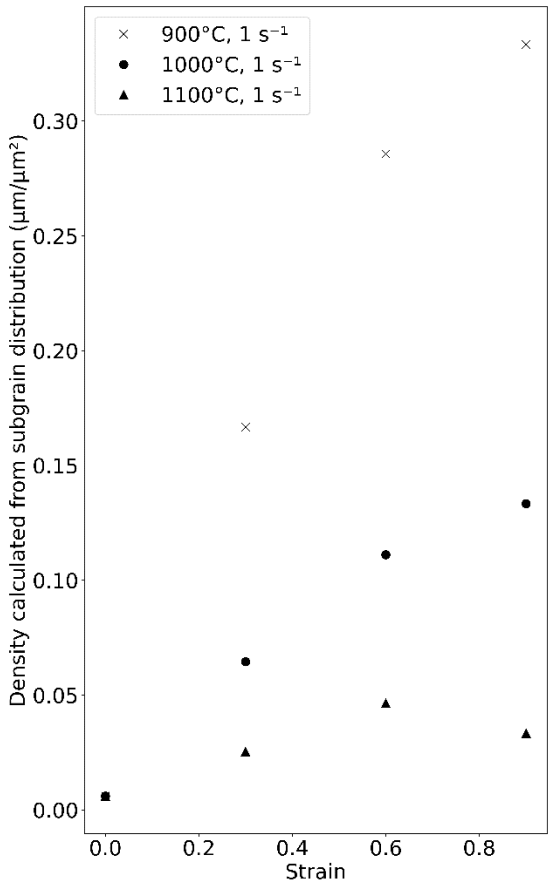

a) S_{Local} *(µm^{-1}) for different deformations and temperatures*

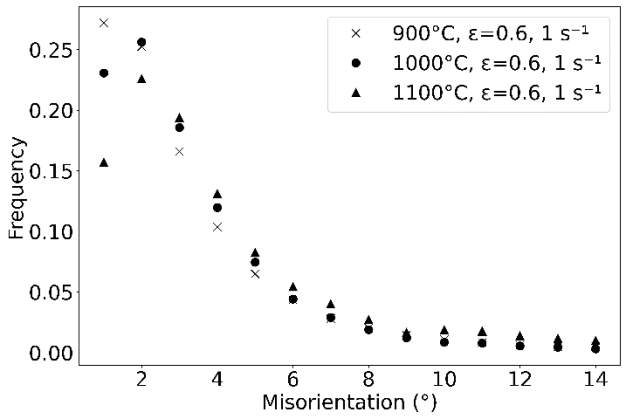

c) Misorientation distribution at $\varepsilon = 0.6$

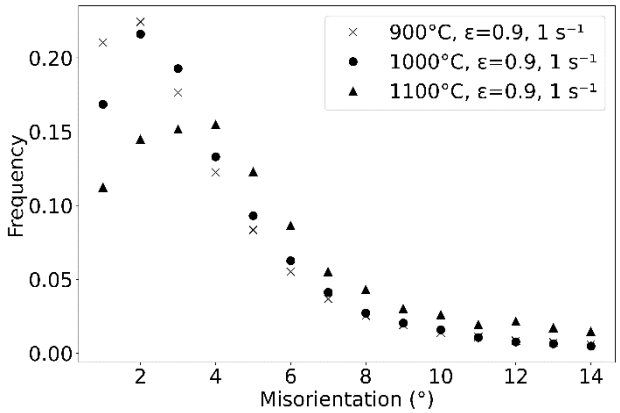

d) Misorientation distribution at $\varepsilon = 0.9$

Figure 9: Evolution of S_{Local} (µm^{-1}) *–a) - Evolution of misorientation distribution for ε=0.3 –b) - Evolution of misorientation distribution for ε=0.6 –c) - Evolution of misorientation distribution for ε=0.9 –d) for hot deformation at 900, 1000 and 1100 °C with 1 s^{-1} strain rate. The LAB density is calculated by considering subgrains of the first mode between 1 and 14° inclusive. The misorientation distribution is calculated by determining the pixel-by-pixel misorientation, for misorientations between 1 and 14° inclusive.*

In Figure 9a, S_{Local} follows a trend comparable to the total LAB density S reported in Figure 4a. The density monotonously increases with an increasing strain and a decreasing temperature. A saturation regime also occurs when examining the population of closed subgrains, consistent with the quantified results in Figure 4. a and Figure 9. a.

The shape of the misorientation distribution $\varphi(\theta)$ (Figure 9. b-d) is slightly different from the previously characterized distribution. The average misorientations are more important: for example, at 900°C, 3, 3.2, and 3.6 ° respectively for 0.3, 0.6, and 0.9 against 1.8, 2.3, and 3 ° in Figure 4. b-d. Therefore, subgrains from the first mode are composed of LAB having a larger misorientation angle. This higher misorientation combined with a proximity to the grain boundaries could result in potential nucleation sites for recrystallization. The subsequent modeling work will be carried out with a specific focus on these subgrains.

Application to the CDRX model

The CDRX model is used [1], [14], [15], [25] to describe the evolution of the LAB density and misorientation as a function of strain. It has been shown in various works that this model works well to describe the LAB population in the steady state regime for very large strain. In such conditions, the LAB network is quite homogeneously spread over the microstructure, making it possible to capture the different mechanisms with a mean-field model. However, in the current work, the model is applied to analyze experimental data during the transient stage of hot deformation, as the LAB is likely not yet stabilized. This approach is more challenging, as the model may result in lower accuracy due to the LAB density heterogeneities reported in the previous section. To take into account these differences, two additional parameters are introduced, c_1 and c_2 (i.e. equations 5-8). The deviations measured by c_1 and c_2 correspond to deviations from n and v_{HAB} (i.e. equations 5-8), which are adjustable parameters in the original model. These two parameters will be able to capture numerical deviations from the usual values of n and v_{HAB} reported in the literature [1], [4], [13]. The aim is to reduce errors in both the experimental misorientation distribution and the LAB density in the microstructure compared to the model and then to discuss any discrepancy in the model parameters. The values n=3 and $v_{HAB} = 10^{-6}$ m.s^{-1} will be considered as reference values, often found in the literature [1], [4], [25]. The parameter α, from the original model, can vary between 0 (exclusive) and 1 (exclusive). The method employed to optimize the parameters is basin hopping [26], which is a two-stage method that combines a global stepping algorithm with local minimization at each step.

Figure 10 outlines the different steps of the numerical tracking process. Two experimental datasets are considered for the optimization: one with the total LAB density (S_{tot}) and the other with the LAB density of the first mode discriminated using the Gaussian Mixture Model (S_{Local}). Similarly, we analyze the misorientation distribution associated with both total LAB density (φ_{tot}) and LAB density from the Gaussian Mixture Model (φ_{Local}), corresponding to the misorientation distribution determined for the first subgrain size mode. Input parameters include values of $h(T, \dot{\varepsilon},)$ and $r(T, \dot{\varepsilon})$ determined from Equations 3 and 4, given in Table 2. D_0, the initial grain size (80 μm), α, c_1, and c_2 are adjustment parameters for minimization. T={900, 1000, 1100} °C and $\dot{\varepsilon} = 1\ s^{-1}$. The initial dislocation density value ρ_0 is determined from the elastic limit σ_0 (Figure 1) using the following equation [27]:

$$\sigma_0 = M\alpha\mu b\sqrt{\rho_0} \tag{9}$$

With M, α, adimensional parameters, μ elastic shear modulus (Pa), b burger vector (m). The CDRX model is then applied (Equations 2, 5, 6, 7, and 8), and the model is iteratively applied up to the desired strain (0.3, 0.6, or 0.9) and calculates the differences between simulated and experimental LAB density and misorientations distributions.

This process goes on until a global minimum of the cost function F_{Min} of the system is reached for a specific α, c_1, and c_2. F_{Min} can be written as:

$$F_{Min} = \sum_{\varepsilon=\{0.3,0.6,0.9\},\ i=\{tot,\ local\}}^{\varepsilon,\ i} \left|S_i - S_{i,sim}\right| + \left|\varphi_i(\theta) - \varphi_{i,sim}(\theta)\right| \tag{10}$$

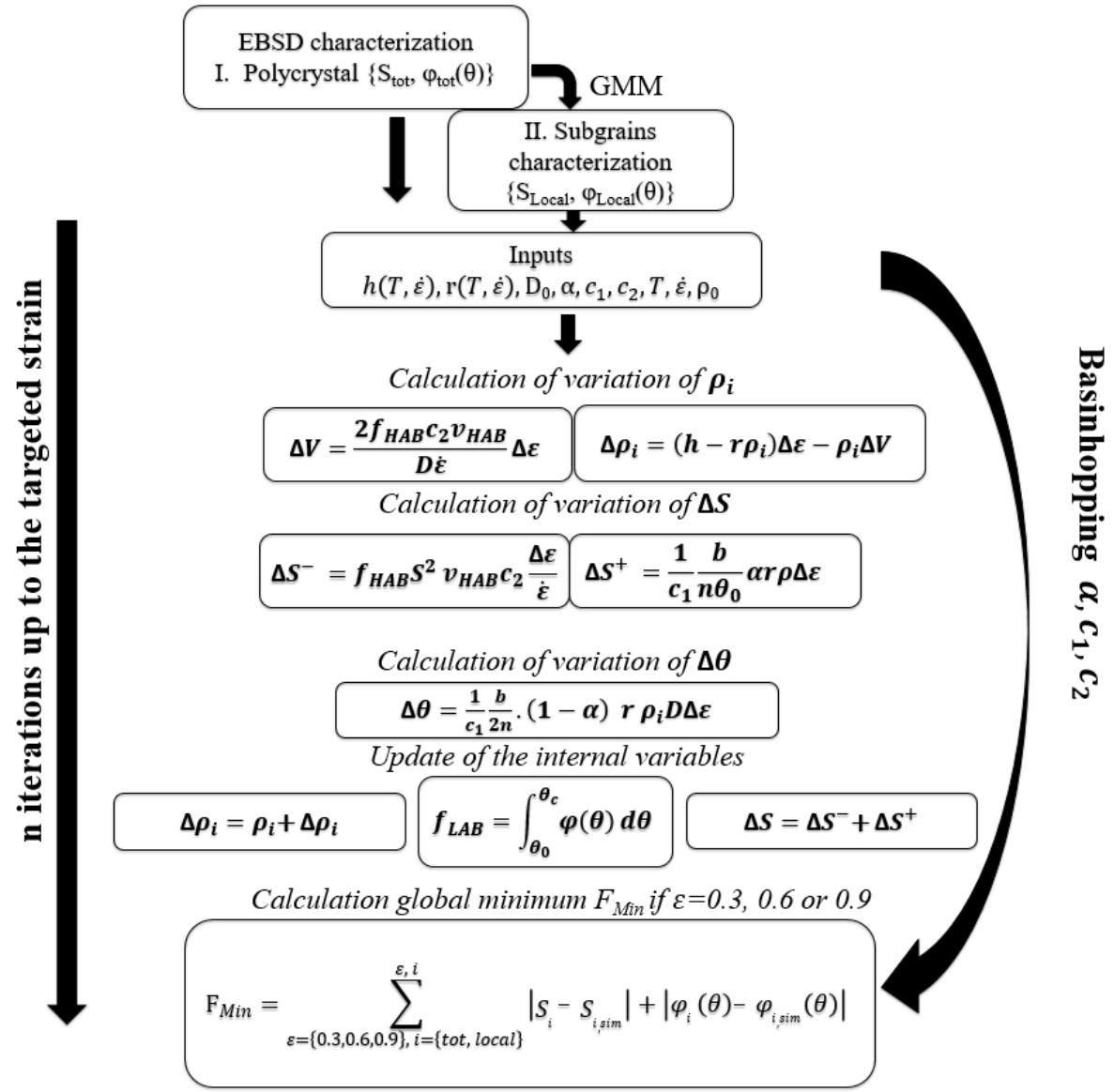

Figure 10: Calculation sequence for the presented model and optimization.

Outputs of interest of the model are the variations obtained of $S_{i,sim}$ and $\varphi_{i,sim}(\theta)$ for the different temperatures and strains applied.

As a first step, it is proposed to test the model with classical values that can be found in the literature (corresponding to values of c_1=1; c_2=1 fixed, only α can vary). The results are shown in Figure 11, and the output for 900 °C is compared with the experimental results (solid line, 'classic approach'). The misorientation distribution is in fairly good agreement but a discrepancy is observed in terms of LAB density, particularly the saturation regime is not predicted by the model. The optimized value for α is found to be 0.3.

A more accurate description is achieved when c_1 and c_2 are included in the parameters to optimize. Their values are summarized in

Table 5. In this case, both the evolution of substructure and misorientation distribution are accurately predicted (Figure 11. a.b).

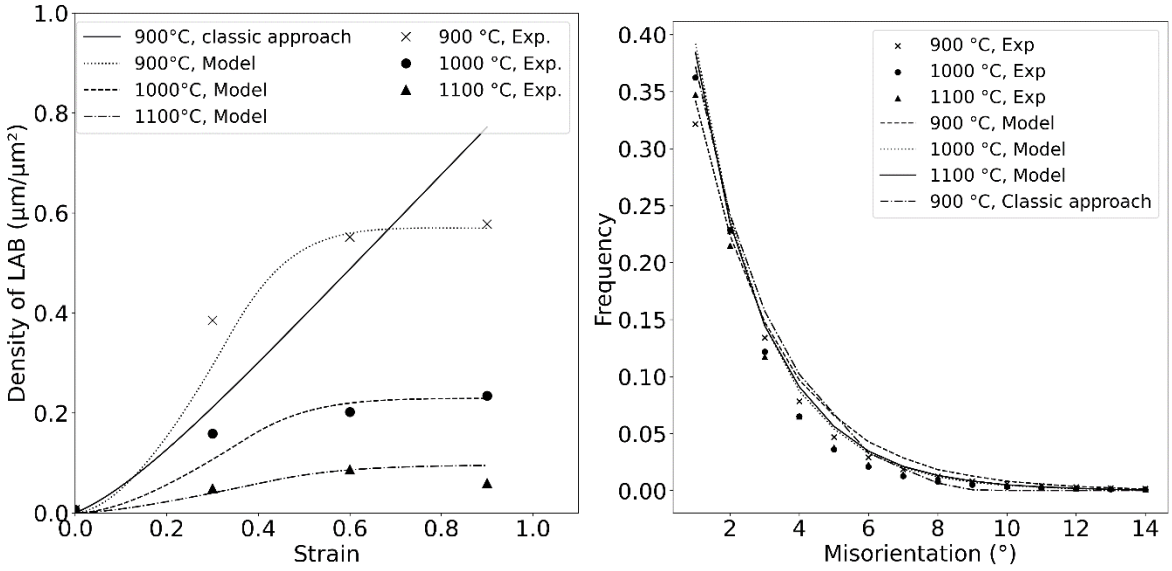

a) *Numerical comparison with experimental LAB density (μm^{-1}) in the case of c_1=1 and c_2=1 (classic approach) and optimization*

b) *Numerical comparison with experimental misorientation distributions in the case of c_1=1 and c_2=1 (classic approach) and optimization. Mean misorientation distributions are represented on this graph.*

Figure 11: Numerical application and comparison of misorientation distribution and LAB density for S_{tot} and φ_{tot}

Table 5: Parameters (α,c_1, c_2) of eq (3) and (4) determined from the optimization process

Parameters	900 °C	1000 °C	1100 °C
Considering all LAB			
α	0.29	0.33	0.32
c_1	0.62	1.50	3.4
c_2	2.5×10^3	2.0×10^4	3.1×10^4
Considering only LAB in the first subgrain distribution			
α	0.26	0.26	0.22
c_1	1.51	2.26	3.54
c_2	1.3×10^3	5.0×10^3	8.0×10^3

The same model is applied to the first distribution of subgrains identified near grain boundaries. The values of φ_{Local} and S_{Local} of Figure 9 are used to identify the model parameters. The parameter values are provided in the second part of Table 5. A difference can be noticed in the

numerical parameters, namely α, c_1, and c_2, depending on the system being considered: { S_{tot}, φ_{tot} } or { S_{Local}, φ_{Local} }. Specifically, c_1 (and c_2) is less important (respectively, more important) when solely considering the first mode of subgrains. For instance, at 900°C, c_1 and c_2 are measured at 0.62 and 2.5×10^3, respectively, in contrast to 1.51 and 1.3×10^3. The increase in c_2 results in a higher annihilation of the substructure by the term dS^- in Equation 8, resulting in a correct description of the LAB densities in Figure 9 with a saturating regime. Regarding α, there is a slight offset between{S_{tot}, φ_{tot}} and {S_{Local}, φ_{Local}}, with values of 0.3 and 0.26, respectively, with few variations depending on temperatures.

IV. Discussions

From the modeling works, it was shown that the direct application of conventional equations (8) and (9) (c_1=c_2=1) for CDRX resulted in significant discrepancies with the experimental LAB density.

Better adjustments were found by modulating the magnitude of these equations through the introduction of c_1 and c_2. Overall, c_1 values are higher than the unit, meaning that the dS^+ (equation 8) was over-estimated in the original model. The introduction of a c_1 helps to minimize this term, therefore making it possible to predict the LAB density stabilization at ε>0.6. However, a value inferior to the unit was found at 900 °C for the numerical adjustments. This is a clear consequence of a rapid increase in LAB density at 900 °C, for ε=0.3, visible in Figure 11. a. Physical interpretation of parameter c_1 might be attributed to other mechanisms undertaken in the CDRX model, such as dislocations getting annihilated by pairs, which can be taken into account by some authors [4], [14]. Some dislocations may indeed disappear by recovery without affecting either the increase in stored energy dS^+ or the LAB misorientation. However, this scenario is not accounted for in the model, leading to an overestimation of dS^+. To compensate for this, c_1 is increased during parameter optimization. It is to be noted that this parameter increases with temperature, which is consistent with the dependence of pairs annihilation of dislocations with temperature [28]. This point is significant because the determination of the exact contribution of pair annihilation to the LAB formation remains unclear, and it is rarely included in models. [9], [14], [17].

The other parameter of interest, c_2, presents important variations compared to the reference value c_2=1. It was shown that a suitable agreement with the experimental dataset could be achieved only with an increase of three to four orders of magnitude of this parameter. It could be attributed to some possible underestimation of the term dV in the original model, compensated by an increase of c_2 after optimization (equations (6) and (9)). The increase of the c_2 parameter is especially important to achieve a saturating regime for the LAB density in Figure 11a, and such a variation could not be reproduced for low c_2 values close to the unit. The creation of LABs and dislocation density are overestimated by the equations of the original model, and a high c_2 parameter allows a saturation state reached for ε>0.6.

It is to be noticed that such high c_2 values are inconsistent with the migration rate of grain boundaries, with classic values of migration rate (usually in the range 10^{-5}-10^{-6} $m.s^{-1}$ for recrystallization and grain growth (ref). Therefore, the increase in c_2 should not be associated with a sudden increase in v_{HAB} as shown in Equation 8, as such an increase would be difficult to justify physically. Instead, it should be interpreted as resulting from an estimation

discrepancy regarding the local density of LAB cleared by boundary migration. Experimental analysis has revealed a notable increase in LAB density near grain boundaries. Therefore, even a small migration of these boundaries could lead to the capture of a significant amount of LAB via Equation 8, exceeding the predictions of the original model by several orders of magnitude. The increase in c_2 after optimization serves as an indication of the importance of this phenomenon.

Therefore, future works should focus not only on the recovery mechanisms at stake during CDRX but should also emphasize the role of LAB heterogeneities as it affects significantly the predictions.

The physical mechanism behind LAB formation is summarized in Figure 12. As strain increases, the LAB network is formed at the grain boundaries due to the increased strain levels near these boundaries and extends towards the grain center. This leads to the early development of small subgrains near grain boundaries, referred to in this study as the 'first distribution', highlighted in red in Figure 12. As strain continues to increase, dislocations tend to aggregate into cells and subgrains at the grain center, however with a lower density resulting in a loose LAB network. The larger subgrains formed by these boundaries are highlighted in blue. The size of these subgrains is primarily determined by the remaining volume of the grain rather than any inherent ability of the dislocations to condense and thus plays a minor role in subsequent phenomena such as recrystallization. Whether modeling predictions are made at the grain scale or a finer scale near grain boundaries, they are significantly affected by this heterogeneous distribution of LAB. Even slight grain boundary migration can effectively remove a substantial fraction of the LAB, as shown in Figure 12c, resulting in elevated c2 values during the identification step. Future developments will focus on the suitable consideration of these strain gradients inside grains, with a more reliable estimation of the resulting dS+ and dS- terms based on these considerations.

Although this would require a significant reformulation of the CDRX model, it would result in improved predictions of LAB population. However, this improvement comes with the trade-off of having to identify additional parameters. Nevertheless, this ongoing model refinement offers promising insights into the evolution of subgrain size and misorientation during hot deformation, with potential applications in the prediction of recrystallization under both dynamic and static conditions.

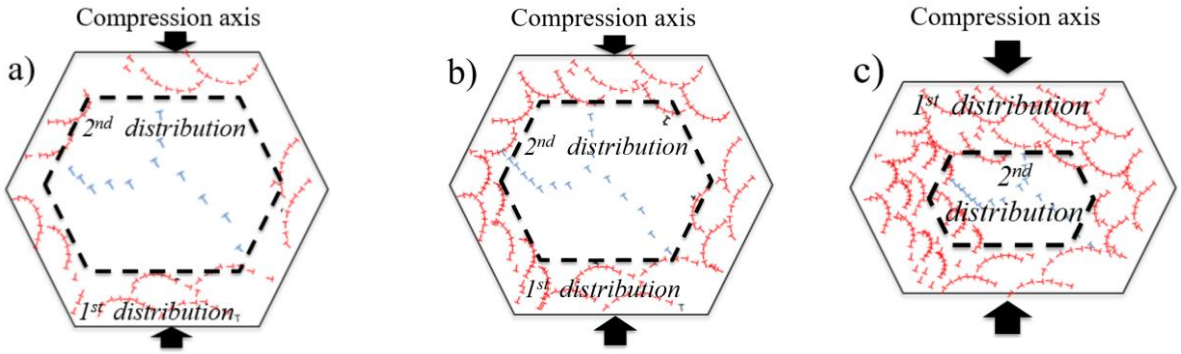

Figure 12: Schematic view depicting the various stages in substructure formation at grain scale during deformation. In red, the first distribution of characterized subgrains in the microstructure, with a smaller, localized average size, was identified near grain boundaries. In blue, the largest subgrains, and/or the remaining undistorted grain, typically located at the core of the grain, represent the second characterized distribution. The two mentioned distributions refer to the identification made in III.c.

V. Conclusions

The substructure evolution of a model ferritic stainless steel close to AISI 430 undergoing continuous dynamic recrystallization is quantified from statistically representative large-scale EBSD mapping.

- LAB density is assessed by EBSD maps, which show a heterogeneous distribution throughout the grain volume. Within the grains, the microstructure can be classified into two groups. The first group, located near grain boundaries, is populated by well-defined subgrains characterized by a size distribution following a log-normal law. These subgrains exhibit significantly higher levels of misorientation compared to the general microstructure. The remainder of the grain volume contains a lower LAB density, forming a loosely connected network of subgrains.

- While the heterogeneous distribution of LAB is well documented in the literature, the quantification of this heterogeneity is often overlooked. This study presents a robust method for identifying these two LAB families using a probabilistic Gaussian mixture model. This novel approach allows for a clear separation of the two populations without the need to manually set a threshold size. As a result, the method facilitates the deconvolution of the subgrain size distribution without relying on user-dependent parameters.

- An improved CDRX model was developed to predict the evolution of LAB density and misorientation distribution. It was found that the model yielded significantly improved predictions when the two equations governing LAB creation and destruction were regulated by parameters that modulate their amplitudes. This study proposes a systematic optimization of these parameters using a cost function that takes into account both the LAB density and the misorientation distribution. The optimization process revealed that achieving a satisfactory agreement with experimental data required specific parameter values that deviated from typical physical limits. This deviation emphasizes the contributions of mechanisms typically overlooked in conventional CDRX models, such as LAB density gradients or potential additional dislocation recovery mechanisms.

The integration of modeling and experimental quantifications suggests that the explicit inclusion of strain gradients within grains could lead to substantial improvements in model predictions while maintaining the integrity of more physical parameter values.

Data availability

The raw/processed data required to reproduce these findings cannot be shared at this time due to legal reasons.

Acknowledgments

The authors would like to thank Frank Montheillet for the discussions and ideas contributed to the subject, as well as Claire Maurice for the assistance in paper correction and the scientific discussions provided during the writing, and Séverine Girard-Insardi for the assistance provided with hot testing samples.

References

[1] S. Gourdet et F. Montheillet, « A model of continuous dynamic recrystallization », *Acta Mater.*, vol. 51, nº 9, p. 2685-2699, mai 2003, doi: 10.1016/S1359-6454(03)00078-8.

[2] F. J. Humphreys et M. Hatherly, « Chapter 7 - Recrystallization of Single-Phase Alloys », in *Recrystallization and Related Annealing Phenomena (Second Edition)*, F. J. Humphreys et M. Hatherly, Éd., Oxford: Elsevier, 2004, p. 215-IV. doi: 10.1016/B978-008044164-1/50011-6.

[3] T. Sakai, A. Belyakov, R. Kaibyshev, H. Miura, et J. J. Jonas, « Dynamic and post-dynamic recrystallization under hot, cold and severe plastic deformation conditions », *Prog. Mater. Sci.*, vol. 60, p. 130-207, mars 2014, doi: 10.1016/j.pmatsci.2013.09.002.

[4] G. Jacquet, « Etude de la cinétique de recristallisation au cours du laminage à chaud d'aciers inoxydables ferritiques stabilisés », These de doctorat, Saint-Etienne, EMSE, 2013. Consulté le: 17 mars 2023. [En ligne]. Disponible sur: https://www.theses.fr/2013EMSE0716

[5] Y. Li, B. Gu, S. Jiang, Y. Liu, Z. Shi, et J. Lin, « A CDRX-based material model for hot deformation of aluminium alloys », *Int. J. Plast.*, vol. 134, p. 102844, nov. 2020, doi: 10.1016/j.ijplas.2020.102844.

[6] D. G. Cram, H. S. Zurob, Y. J. M. Brechet, et C. R. Hutchinson, « Modelling discontinuous dynamic recrystallization using a physically based model for nucleation », *Acta Mater.*, vol. 57, nº 17, p. 5218-5228, oct. 2009, doi: 10.1016/j.actamat.2009.07.024.

[7] J. Favre, D. Fabrègue, A. Chiba, et Y. Bréchet, « Nucleation of recrystallization in fine-grained materials: an extension of the Bailey–Hirsch criterion », *Philos. Mag. Lett.*, vol. 93, nº 11, p. 631-639, nov. 2013, doi: 10.1080/09500839.2013.833352.

[8] F. Lefevre-Schlick, Y. Brechet, H. S. Zurob, G. Purdy, et D. Embury, « On the activation of recrystallization nucleation sites in Cu and Fe », *Mater. Sci. Eng. A*, vol. 502, nº 1, p. 70-78, févr. 2009, doi: 10.1016/j.msea.2008.10.015.

[9] G. Maizza, R. Pero, M. Richetta, et R. Montanari, « Continuous dynamic recrystallization (CDRX) model for aluminum alloys », *J. Mater. Sci.*, vol. 53, nº 6, p. 4563-4573, mars 2018, doi: 10.1007/s10853-017-1845-4.

[10] L. S. Tóth, Y. Estrin, R. Lapovok, et C. Gu, « A model of grain fragmentation based on lattice curvature », *Acta Mater.*, vol. 58, nº 5, p. 1782-1794, mars 2010, doi: 10.1016/j.actamat.2009.11.020.

[11] S. R. Skjervold et N. Ryum, « Characterization of local texture in a moderately deformed polycrystalline AlSi-alloy », *Acta Metall. Mater.*, vol. 43, nº 8, p. 3159-3176, août 1995, doi: 10.1016/0956-7151(95)00008-J.

[12] D. P. Field, P. B. Trivedi, S. I. Wright, et M. Kumar, « Analysis of local orientation gradients in deformed single crystals », *Ultramicroscopy*, vol. 103, nº 1, p. 33-39, avr. 2005, doi: 10.1016/j.ultramic.2004.11.016.

[13] J.-P. Thomas, « Etude expérimentale et modélisation de l'évolution microstructurale du superalliage 718 en déformation à chaud », These de doctorat, Saint-Etienne, EMSE, 2005. Consulté le: 17 mars 2023. [En ligne]. Disponible sur: https://www.theses.fr/2005EMSE0002

[14] M. C. Poletti, « Continuous dynamic recrystallization during hot torsion of an aluminum alloy. - IOPscience ». Consulté le: 27 juin 2023. [En ligne]. Disponible sur: https://iopscience.iop.org/article/10.1088/1742-6596/1270/1/012049/meta

[15] R. H. Buzolin, F. Krumphals, et M. C. Poletti, « Topological aspects in the microstructural evolution of AA6082 during hot plastic deformation », *Eur. J. Mater.*, vol. 0, nº 0, p. 1-24, sept. 2022, doi: 10.1080/26889277.2022.2125350.
[16] Z. C. Sun, H. L. Wu, J. Cao, et Z. K. Yin, « Modeling of continuous dynamic recrystallization of Al-Zn-Cu-Mg alloy during hot deformation based on the internal-state-variable (ISV) method », *Int. J. Plast.*, vol. 106, p. 73-87, juill. 2018, doi: 10.1016/j.ijplas.2018.03.002.
[17] R. H. Buzolin, F. Krumphals, et M. C. Poletti, « Topological aspects in the microstructural evolution of AA6082 during hot plastic deformation », *Eur. J. Mater.*, vol. 3, nº 1, p. 2218403, déc. 2023, doi: 10.1080/26889277.2022.2125350.
[18] « Essais rhéologiques à chaud », Techniques de l'Ingénieur. Consulté le: 14 février 2024. [En ligne]. Disponible sur: https://www.techniques-ingenieur.fr/base-documentaire/materiaux-th11/mise-en-forme-des-metaux-aspects-rheologiques-et-metallurgiques-42476210/essais-rheologiques-a-chaud-m3009/
[19] F. Pedregosa *et al.*, « Scikit-learn: Machine Learning in Python », *J. Mach. Learn. Res.*, vol. 12, nº 85, p. 2825-2830, 2011.
[20] R. T. DeHoff et F. N. Rhines, « Quantitative microscopy ». Consulté le: 7 septembre 2023. [En ligne]. Disponible sur: https://philpapers.org/rec/DEHQM
[21] A. Laasraoui et J. J. Jonas, « Prediction of steel flow stresses at high temperatures and strain rates », *Metall. Trans. A*, vol. 22, nº 7, p. 1545-1558, juill. 1991, doi: 10.1007/BF02667368.
[22] L. Hennocque *et al.*, « On the Application of some Plasticity Laws », *Solid State Phenom.*, vol. 353, p. 163-168, déc. 2023, doi: 10.4028/p-SXs81M.
[23] F. Montheillet, O. Lurdos, et G. Damamme, « A grain scale approach for modeling steady-state discontinuous dynamic recrystallization », *Acta Mater.*, vol. 57, nº 5, p. 1602-1612, mars 2009, doi: 10.1016/j.actamat.2008.11.044.
[24] S. V. Raj et G. M. Pharr, « A compilation and analysis of data for the stress dependence of the subgrain size », *Mater. Sci. Eng.*, vol. 81, p. 217-237, août 1986, doi: 10.1016/0025-5416(86)90265-X.
[25] S. Gourdet, « Étude des mécanismes de recristallisation au cours de la déformation a chaud de l'aluminium ».
[26] B. Olson, I. Hashmi, K. Molloy, et A. Shehu, « Basin Hopping as a General and Versatile Optimization Framework for the Characterization of Biological Macromolecules », *Adv. Artif. Intell.*, vol. 2012, p. e674832, déc. 2012, doi: 10.1155/2012/674832.
[27] Z. S. Basinski, « Thermally Activated Glide in Face-Centred Cubic Metals and its Application to the Theory of Strain Hardening », *Philos. Mag.*, vol. 4, nº 40, p. 393-432, 1959, doi: 10.1080/14786435908233412.
[28] T. Yu, « DEFORMATION MICROSTRUCTURE AND RECOVERY ».